Deep-learning assisted regularized elastic full waveform inversion using the velocity distribution information from wells

Yuanyuan Li [ORCID], Tariq Alkhalifah and Zhendong Zhang [ORCID]*

Physical Science and Engineering Division, King Abdullah University of Science and Technology, 4700 *KAUST, Thuwal 23955–6900, Kingdom of Saudi Arabia. E-mail:* yuanyuan.li@kaust.edu.sa

SUMMARY

Elastic full waveform inversion (EFWI) can, theoretically, give high-resolution estimates of the subsurface. However, in practice, the resolution and illumination of EFWI are limited by the bandwidth and aperture of seismic data. The often-present wells in developed fields as well as some exploratory regions can provide complementary information of the target area. We, thus, introduce a regularization technique, which combines the surface seismic and well log data, to help improve the resolution of EFWI. We use deep neural networks to learn the statistical relations between some selected features of the inverted model and the facies interpreted from well logs. The selected features are the means and variances of the inverted velocities defined within Gaussian windows. Using multiple fully connected layers, we train our neural networks to identify the relation between the means and variances at the well location and those from the inverted model. The network is used to map the means and variances extracted from the well to the whole model domain. We then perform another EFWI in which we fit the predicted data to the observed ones as well as fit the model over a Gaussian window to the predicted means and variances. The tests on synthetic and real seismic data demonstrate that the proposed method can effectively improve the resolution and illumination of deep-buried reservoirs, which often encounter poor illumination from seismic data.

Key words: Image processing; Inverse theory; Waveform inversion; Seismic tomography.

INTRODUCTION

Reservoir characterization plays an essential role in exploration and development, specially in evaluating the potential for hydrocarbon reservoirs and positioning the drilling well (Eidsvik *et al.* 2004; Gao 2011). The principal objective of reservoir characterization is representing a reservoir quantitatively using integrated data from a variety of sources and disciplines (Fanchi 2002). Amplitude versus offset (AVO) analysis is a well-known seismic inversion technique for prediction of reservoir properties from seismic data (Buland & Omre 2003; Veeken & Rauch-Davies 2006). Although these AVO techniques have generally served us well over the years, they rely on the quality of the migrated image, which in turn depends on the estimated velocity model. Full waveform inversion (FWI) has shown its high potential in describing the subsurface properties with high resolution by using the full wavefield and fitting the observed data directly (Bamberger *et al.* 1982; Lailly 1983; Tarantola 1984; Gauthier *et al.* 1986; Pratt *et al.* 1998; Virieux & Operto 2009; Routh *et al.* 2017; Zhang & Alkhalifah 2019b; Li *et al.* 2020).

Elastic full waveform inversion (EFWI) aims to estimate the elastic properties with reasonably high resolution in hope of providing information useful for reservoir characterization (Vigh *et al.* 2014; Naeini *et al.* 2016). One of the critical challenges for EFWI is the cycle-skipping issue arising from the lack of low frequencies and an inaccurate starting model, which prompted many proposed solutions (Bunks *et al.* 1995; van Leeuwen & Herrmann 2013; Alkhalifah 2014; Wu *et al.* 2014; Warner & Guasch 2016; Li *et al.* 2018, 2019; Ovcharenko *et al.* 2019; Zhang & Alkhalifah 2019a; Song *et al.* 2020). Here, we focus on high-resolution delineation of the subsurface elastic properties. Seismic data often admit incomplete subsurface information with limited model wavenumber information due to limitations associated with surface seismic data in terms of the signal-to-noise ratio (SNR), frequency band, aperture and coverage (Sirgue & Pratt 2004; Alkhalifah 2016). Furthermore, model building solely from surface seismic data is severely ill-posed when multiple parameters are required to describe the subsurface. Such inherent limitations of seismic data can be mitigated by integrating data from other geophysical surveys and disciplines. Using the Bayesian framework, we can complement seismic data with geologic information and rock-physics knowledge as we estimate the velocity, thus improving the consistency of the inverted model with the underlying geologic and lithologic assumptions (Curtis &

*Now at: Department of Geosciences, Princeton University, NJ 08540, USA

Lomax 2001; Zunino *et al.* 2015; Li *et al.* 2016; Zhang *et al.* 2018; Aragao & Sava 2020). Borehole data, which includes well logs, check shots, and vertical seismic profiles, show promising complementary information to seismic data to reduce the ill-posedness of the inverse problem (Asnaashari *et al.* 2013; Wang *et al.* 2013; Zhang & Alkhalifah 2019b). Some successfully implemented AVO techniques also include both seismic and well data to obtain geologically plausible models, where well data serve as the constraints of the inverse problem (Bosch *et al.* 2009, 2010; Grana 2016; Zabihi Naeini & Exley 2017).

High-resolution well logs can compensate for the lack of illumination provided by seismic data where the well is used as a model-space regularizer for waveform inversion (Asnaashari *et al.* 2013; Li *et al.* 2021). Well logs provide reliable and detailed information of the subsurface, but only sample very limited areas. The key problem is how to link the high-resolution well information to the subsurface model estimated from EFWI. Asnaashari *et al.* (2013) built an *a priori* model by interpolating the well velocities and gradually decreasing the weight of the prior model during inversion. Zhang *et al.* (2018) employed Bayesian theory to invert for a facies map by maximizing the posterior probability using the L2-norm inversion result and the predetermined facies information from well data. In a similar way, Singh *et al.* (2018) constrain the inversion workflow using the prior model derived from the facies distribution and the available well logs. Aragao & Sava (2020) developed an elastic FWI algorithm constrained by petrophysical information extracted from well logs to guide the inversion toward realistic lithology. Zhang & Alkhalifah (2019b) improve the incorporation of facies information using deep neural networks (DNNs).

Machine learning (ML) techniques have been applied to solve problems in geophysics for decades (Dowla *et al.* 1990; Dysart & Pulli 1990; Dai & MacBeth 1995). Considering the recent advances in high-performance computing and the availability of powerful numerical algorithms, the applications of ML is on a steep rise in recent years (Bergen *et al.* 2019). Deep learning (DL; LeCun *et al.* 2015), as a branch of ML, demonstrated great potential in tackling a broad range of tasks, that include feature representations (Qian *et al.* 2018), classification of seismic events and facies (Kortström *et al.* 2016; Zhao *et al.* 2017) and more. Deep learning is capable of predicting the subsurface model directly from the seismic data as well (Richardson 2018; Araya-Polo *et al.* 2019; Kazei *et al.* 2019; Yang & Ma 2019). The combination of well data and seismic information for estimating subsurface properties has motivated the development of the following DL-based techniques. Das *et al.* (2019) augmented the data set based on the well logs and provided a statistically similar labelled training data set for a convolutional neural network (CNN) to infer seismic impedance. The impedance was predicted by a fully convolutional residual network (FCRN) trained by the data set generated from a synthetic model and further optimized by transfer learning with well information (Wu *et al.* 2020). Zhang & Alkhalifah (2019b; 2020) employed DNNs to build the proper statistical connection that converts seismic estimates to facies interpreted from well logs. They use v_p, v_s and their ratio as discriminant features of facies extracted from well logs. However, the neural network predictions tend to capture averaged model parameters within layers, and the high-resolution components of well velocities were hard to preserve because of the averaged properties within facies. To retain the high-resolution information of well logs, we include the mean and variance of v_p and v_s, computed in a Gaussian window, as the discriminant features. The derived high-resolution prior model is added to EFWI as a regularization term (Li *et al.* 2020).

In this paper, we combine seismic data and well logs in an EFWI scheme regularized by an *a priori* model using deep learning to boost the illumination and resolution of the subsurface properties. We start by conducting a conventional EFWI to obtain the inverted *P*- and *S*-wave velocities. Then, we design and train a DNN to learn the statistical relations between the inverted model and the facies interpreted from well logs featured by the mean and variance of velocities. The mean and variance of velocities for the whole model can be predicted using the trained network. Finally, we perform EFWI regularized by the prior model, which is recovered from the mean and variance field. The synthetic data from an Otway model and a 2-D ocean-bottom-cable (OBC) field data are used to demonstrate the effectiveness of the proposed method.

THEORY

Regularized elastic FWI

FWI attempts to retrieve the subsurface model properties by minimizing the residuals between the simulated and observed seismograms using an iterative local-optimization scheme. In our EFWI, we invert for the *P*- and *S*-wave velocities simultaneously and keep the density fixed, under the isotropic assumption. The optimization problem over the often enormous solution space using band-limited seismic data admits strong nonlinearity and non-uniqueness. These limitations can be alleviated by utilizing regularization techniques, which render a solution that also satisfies some prior characterizations. The objective function for a regularized EFWI can be defined as

$$J(\mathbf{m}) = J_D(\mathbf{m}) + \beta R(\mathbf{m}), \tag{1}$$

where $J_D(\mathbf{m})$ is the data misfit term, $R(\mathbf{m})$ is the regularization term and β is a weighting parameter balancing the contributions from these two terms. $J_D(\mathbf{m})$ is often given by the L2 norm of the data residuals:

$$J_D(\mathbf{m}) = \|\mathbf{W}_d (\mathbf{d}(\mathbf{m}) - \mathbf{d}_o)\|_2^2, \tag{2}$$

where $\mathbf{d}(\mathbf{m})$ denotes the predicted data determined by the model $\mathbf{m}$ using the elastic wave equation, $\mathbf{d}_o$ is the observed seismic data and $\mathbf{W}_d$ is a diagonal weighting matrix for the seismic data, which can be related to the data reliability information.

To preserve the sharp geological interfaces, a total variation (TV; Lin & Huang 2014) regularization is often used, and it is given by

$$R_{\mathrm{TV}}(\mathbf{m}) = \|\mathbf{m}\|_{\mathrm{TV}} = \sqrt{\mathbf{m}_x^2 + \mathbf{m}_z^2}, \tag{3}$$

where $\mathbf{m}_x$ and $\mathbf{m}_z$ represent the components of the model gradient. If reliable model information in the target zone is available, this prior information can constrain the inversion process by penalizing the model deviations from the prior. The corresponding regularization term is then defined to measure the misfit between the updated and prior models:

$$R_{\mathrm{prior}}(\mathbf{m}) = \left\|\mathbf{W}_m (\mathbf{m} - \mathbf{m}_{\mathrm{prior}})\right\|_2^2, \tag{4}$$

where $\mathbf{W}_m$ is a diagonal weighting matrix for the prior model, $\mathbf{m}_{\mathrm{prior}}$ refers to the prior model, which can incorporate, for example, well information. In our case, $\mathbf{m}_{\mathrm{prior}}$ is recovered from the mean and variance fields, which are predicted by a DNN.

The model is updated iteratively to minimize the objective function using the following formula:

$$\mathbf{m}_{k+1} = \mathbf{m}_k + \alpha_k \mathbf{H}^{-1} \mathbf{g}_k, \tag{5}$$
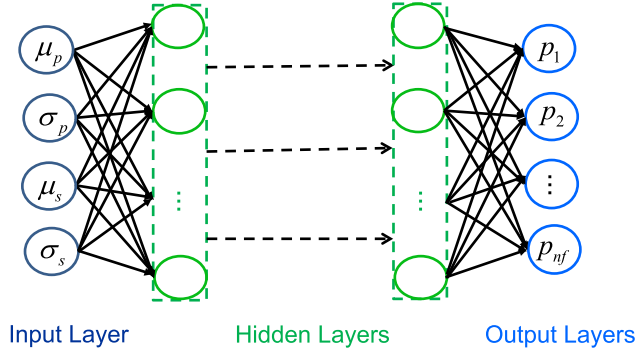
Figure 1. The architecture of the deep neural network (DNN). The DNN consists of input and output layers, with fully connected hidden layers in between. The input features for the input layer include the means and variances of v_p and v_s, defined in a Gaussian window, i.e. $(\mu_p, \mu_s, \sigma_p, \sigma_s)$. The output layer holds the probabilities $(p_1, \cdots, p_i, \cdots, p_{nf})$ of being categorized into each of the facies.

where the subscript (k) refers to the iteration number in FWI, α_k is the step length, $\mathbf{g}_k$ is the gradient of the objective function with respect to the model parameters and $\mathbf{H}^{-1}$ is the approximate inverse Hessian matrix estimated here using the L-BFGS algorithm (Byrd *et al.* 1995). The gradient of the objective function, which involves a prior model regularization term, is given by

$$\mathbf{g} = \frac{\partial J(\mathbf{m})}{\partial \mathbf{m}} = \frac{\partial \left(J_D(\mathbf{m}) + \beta R_{\mathrm{prior}}(\mathbf{m}) \right)}{\partial \mathbf{m}},$$
$$= \left(\frac{\partial \mathbf{d}(\mathbf{m})}{\partial \mathbf{m}} \right)^T \mathbf{W}_d^T \mathbf{W}_d \left(\mathbf{d}(\mathbf{m}) - \mathbf{d}_o \right)$$
$$+ \beta \mathbf{W}_m^T \mathbf{W}_m \left(\mathbf{m} - \mathbf{m}_{\mathrm{prior}} \right). \tag{6}$$

The regularization parameter β balances the contributions from the data and the prior knowledge. To guarantee the comparability of these two terms, β is evaluated using the following formula:

$$\beta = \gamma \frac{\left\| \mathbf{W}_d \left(\mathbf{d}(\mathbf{m}) - \mathbf{d}_o \right) \right\|_2^2}{\left\| \mathbf{W}_m \left(\mathbf{m} - \mathbf{m}_{\mathrm{prior}} \right) \right\|_2^2}, \tag{7}$$

where γ is a dimensionless weighting factor and it can be adjusted to comply with the reliability of the prior information. Our numerical tests indicate that a value between 0.3 and 0.6 is acceptable, leaning towards the higher value (0.6) if we have a relatively well-predicted prior model and the quality of the seismic data is poor.

DNN-assisted *a priori* model building

The classic EFWI application only retrieves limited model information from the band-limited seismic data. Well logs contain much higher resolution information, but they often represent a very limited spatial area. These wells can be utilized as *a priori* information to enhance the model resolution from surface seismic data. The often complicated relation (upscaling) between surface seismic inverted models and the well information can be formed by training a DNN. An *a priori* model can be derived by a neural network that maps the inverted model to the interpreted facies from wells.

A DNN is given by optimized mathematical manipulations to convert inputs to specific output, and it is capable of representing complex nonlinear relationships (Schmidhuber 2015). The neural network consists of input and output layers, with fully connected hidden layers in between. The architecture we are using is shown in Fig. 1. The data flows from the input layer, through the hidden
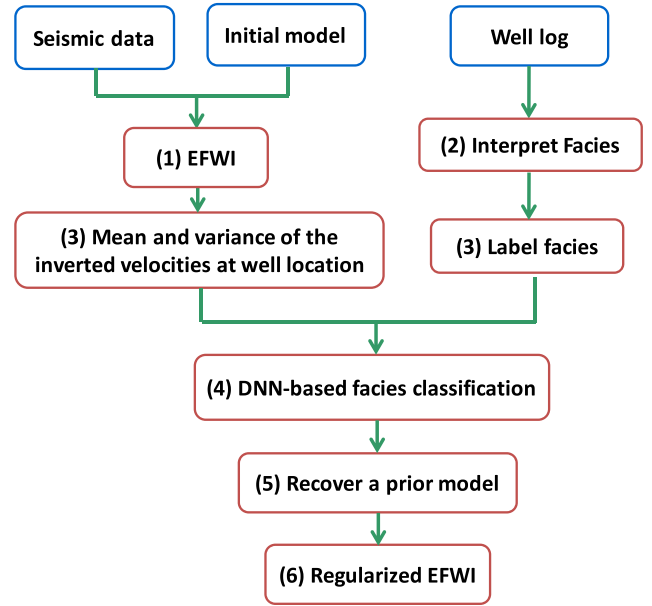

Figure 2. The inversion workflow for the proposed inversion method. The inputs for the workflow are shown in the blue boxes; the numbers in the red boxes correspond to the step numbers outlined at the end of the theory part.

layers, and to the output layer in a feedforward fashion. For a vector of inputs $\mathbf{a}_0$, a general forward-propagation equation is described as $\mathbf{a}_l = g_l(\mathbf{W}_l \mathbf{a}_{l-1} + \mathbf{b}_l)$, where $\mathbf{W}_l$ and $\mathbf{b}_l$ refer to the weighting matrix and the bias vector for the lth layer, respectively. The activation function g_l is used to induce nonlinearity in the formulation. Here, we employ rectified linear unit (Relu) and softmax activation function for the hidden layers and the output layer, respectively (Nair & Hinton 2010). The softmax function admits a probability distribution of the classes of facies. For the training process, we first initialize the weights and biases randomly and then update them using the Adam optimizer, with the loss function given by the sparse cross entropy (Kingma & Ba 2014). The number of hidden layers and neurons of each layer is adjusted according to the size of the training data set. Details of the DNN used in each example will be shared in the examples sections.

Training a DNN requires inverting for a large number of parameters (weights and biases) that defines the network, which in turn requires a large training data set and techniques to prevent overfitting (Bergen *et al.* 2019). To expand the training data set, the estimated velocities close to the well locations can serve as training data considering the often lateral continuity of many features around the well, especially at the surface seismic scale. Besides, we apply a synthetic minority over-sampling technique (SMOTE) to enlarge the training data sets and reduce the imbalance of different facies (Chawla *et al.* 2002). We also employ a random dropout of 30 per cent to avoid overfitting (Srivastava *et al.* 2014).

To prepare the training data set for supervised learning, we label the selected training samples from the inverted model using the corresponding facies interpreted from well logs. The samples from well logs with a similar statistical distribution, defined in a Gaussian window, are interpreted as a single facies. We specifically calculate the mean (μ) and variance (σ) to represent the statistical distribution. In this case, the variance captures the high-resolution features of the well, while the mean provides the average value. The DNNs-based classification of facies is implemented by discriminating the selected features of the facies. We use means and
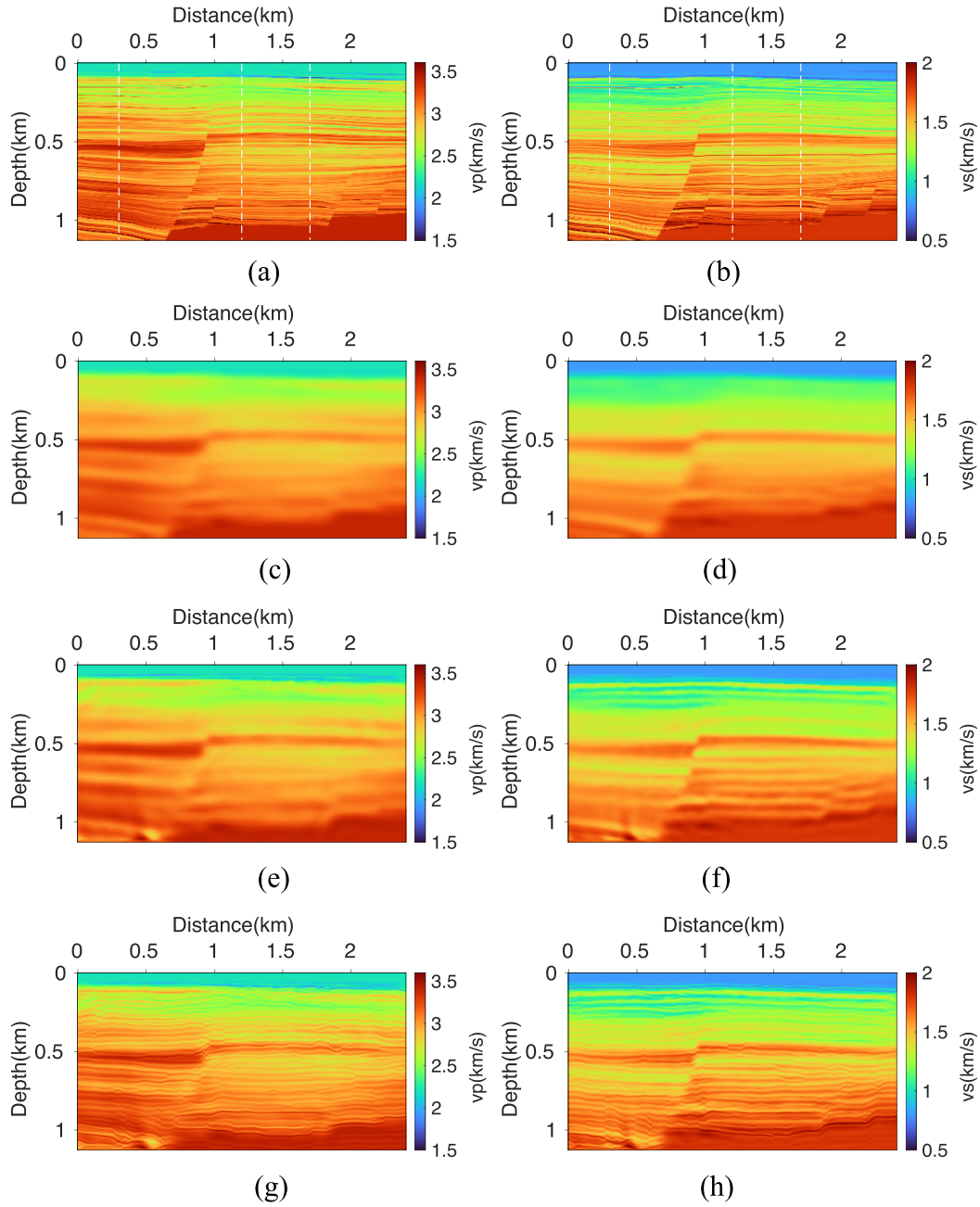
Figure 3. (a and b) The true v_p and v_s model for the Otway example, and the white dashed lines show the well locations. (c and d) The initial v_p and v_s model. (e and f) The conventional EFWI result using 2–15 Hz frequency band after 80 iterations: (e) v_p and (f) v_s. (g and h) The regularized EFWI result using the proposed method: (g) v_p and (h) v_s.

variances of v_p and v_s, defined in a Gaussian window, as the discriminant or input features, i.e. (μ_p, μ_s, σ_p, σ_s). Interpreted facies from the well logs are used as the labels in the training. Once this training is finished, the DNN establishes a mathematical connection between the features of inverted model and various facies classes. We can apply the network to the whole inversion region to predict the facies (given by the means and variances from the well) distribution for every model point. The output for every point is a single vector $p = (p_{1,\cdots}, p_{i,\cdots}, p_{nf})$, in which each element represents a probability that this model point is categorized as facies i, and this probability was provided by the softmax activation function applied to obtain the output layer. Thus, we predict the mean and variance

for each point as the expected value instead of the specific value with highest probability. The predicted mean and variance fields using a weighted average are smoother than those using the highest probability, which conforms to our expectation because the mean and variance are defined in a Gaussian window. Given the probability distribution, we can compute the expected value by a weighted average over facies representing the predicted features (means and variances) as follows:

$$\left(\bar{\mu}_p, \bar{\mu}_s, \bar{\sigma}_p, \bar{\sigma}_s\right) = \sum_{\mathrm{nface}} p_i \left(\mu_p{}^i, \mu_s{}^i, \sigma^i{}_p, \sigma^i{}_s\right), \qquad (8)$$
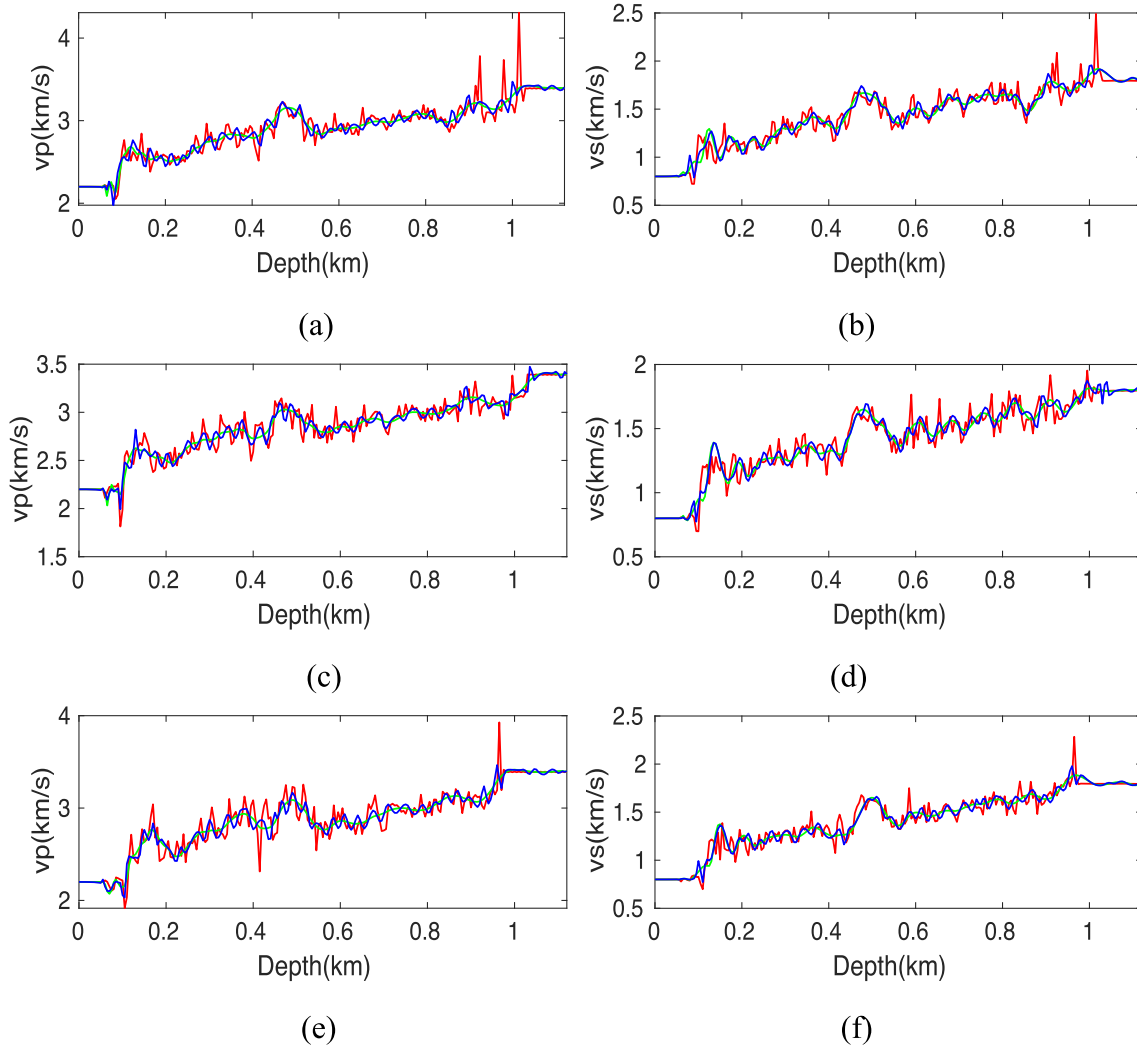
Figure 4. Comparison of v_p and v_s vertical profiles at distance of (a and b) 1 km, (c and d) 1.5 km and (e and f) 2 km. These profiles are not used as training wells. Red line: the true model, green line: the conventional EFWI result shown in Figs 3(e) and (f) using 2–15 Hz, blue line: the regularized EFWI result in Figs 3(g) and (h) using the proposed method with 2–15 Hz.
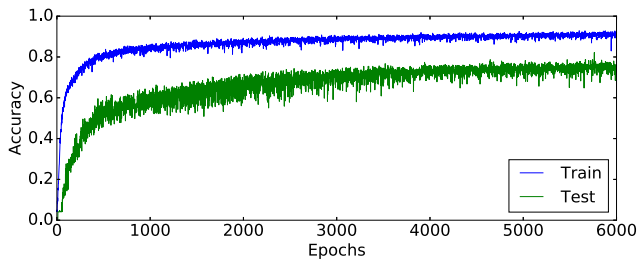
Figure 5. The history of the training and test accuracies in the training process with the total of 6000 epochs. A total of 92.16 per cent training loss is achieved, while the test accuracy stays at approximately 74.57 per cent.

where p_i and $(\mu_p{}^i, \mu^i{}_s, \sigma^i{}_p, \sigma^i{}_s)$ are the predicted probability and the feature vector for facies i, respectively.

With the predicted mean and variance fields, the high-resolution prior model can be recovered by solving the following optimization problem:

$$
\begin{aligned}
\mathbf{m}_{\mathrm{prior}} = \arg\min_{\mathbf{m}} \frac{1}{\|\bar{\mu}\|_2^2} & \left\| \int_{-w_s, w_s} m(x, z+\tau) \right. \\
& \times \mathrm{gau}(\tau)\,\mathrm{d}\tau - \bar{\mu}(x, z) \Big\|_2^2 \\
+ \lambda \frac{1}{\|\bar{\sigma}\|_2^2} & \left\| \int_{-w_s, w_s} (m(x, z+\tau) - \bar{\mu}(x, z))^2 \right. \\
& \times \mathrm{gau}(\tau)\,\mathrm{d}\tau - \bar{\sigma}(x, z) \Big\|_2^2 .
\end{aligned}
\tag{9}
$$

where, $\mathrm{gau}(\tau)$ is a normalized Gaussian smoothing operator with a width w_s. The width w_s and the weighting factor λ are set as 10 and 0.001 in the examples, respectively. The prior model is inverted iteratively using a gradient-based inversion algorithm. Lastly, we implement the regularized EFWI by incorporating the prior model into the inversion scheme.

As a summary, the proposed inversion algorithm is given by the following the workflow, also summarized in Fig. 2:
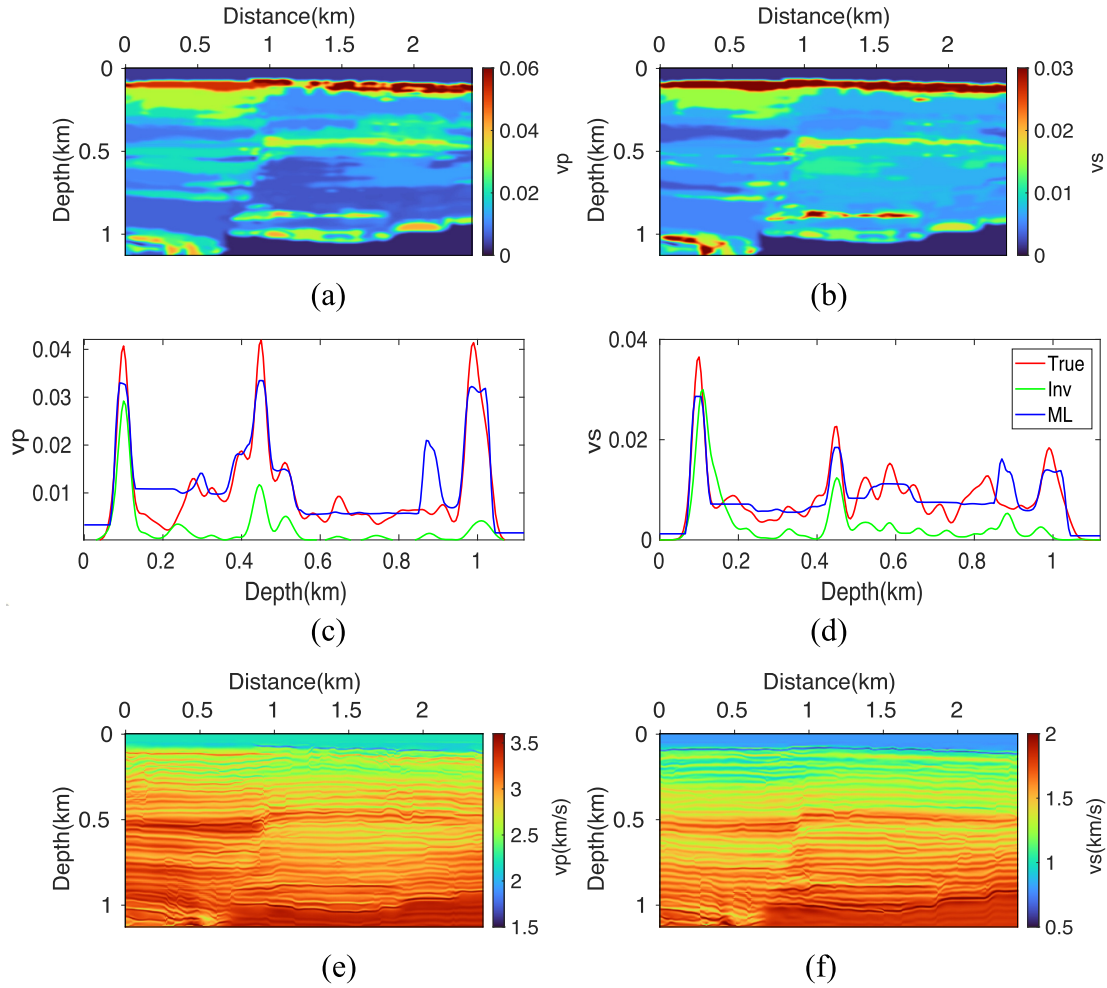
Figure 6. The predicted variance fields for (a) v_p and (b) v_s. (c and d) The comparison of the variance for v_p and v_s at x = 1.2 km (red line: the true variance, green line: the variance computed from the conventional EFWI result in Figs 3(e) and (f), blue line: the predicted variance by using DNNs). (e and f) The recovered prior model from the predicted mean and variance fields: v_p and v_s.

(1) Using the seismic data and an initial model, we conduct a conventional EFWI to invert for the subsurface elastic properties (*P*-wave and *S*-wave velocities) by minimizing the data misfit defined by eq. (2).

(2) Given the well logs as input, we interpret facies from well logs (check shots or sonic) by identifying the velocity means and variances within Gaussian windows.

(3) We then prepare the training data set for optimizing the parameters of our DNN: We compute mean and variance of the inverted velocities generated from step 1 as input features $(\mu_p, \mu_s, \sigma_p, \sigma_s)$, and label the selected training samples from the seismic estimations near the wells using the interpreted facies.

(4) We train the DNN and apply the trained DNN to the whole inverted velocity model from step 1 to predict the probability distribution of facies, featured by the means and variances of the well velocities, and then compute the predicted means and variances using eq. (8). This step corresponds to the DNN-based facies classification in Fig. 2.

(5) Given the predicted means and variances, we recover the prior model by solving eq. (9).

(6) We perform another EFWI (regularized EFWI in Fig. 2) by using the objective function of eq. (1) including the regularization term of eq. (4), in which we fit the predicted data to the observed ones as well as fit the model to the prior model.

NUMERICAL EXAMPLES

We use a synthetic example representing a slice of the realistic Otway model (Glubokovskikh *et al.* 2016) and a 2-D line from the Volve OBC field data (Szydlik *et al.* 2007) to demonstrate the performance of the proposed inversion scheme in elastic media. We invert for *P*- and *S*-wave velocities simultaneously and keep density fixed to 2000 kg m^{-3} during the elastic inversion. In these two examples, we use a staggered-grid finite-difference scheme with 10th-order accuracy in space and second-order accuracy in time to simulate the elastic wave propagation (Virieux 1986). The perfectly matched layer (PML) technique is employed on all sides of the model to absorb the boundary reflections (Zhang & Shen 2010).
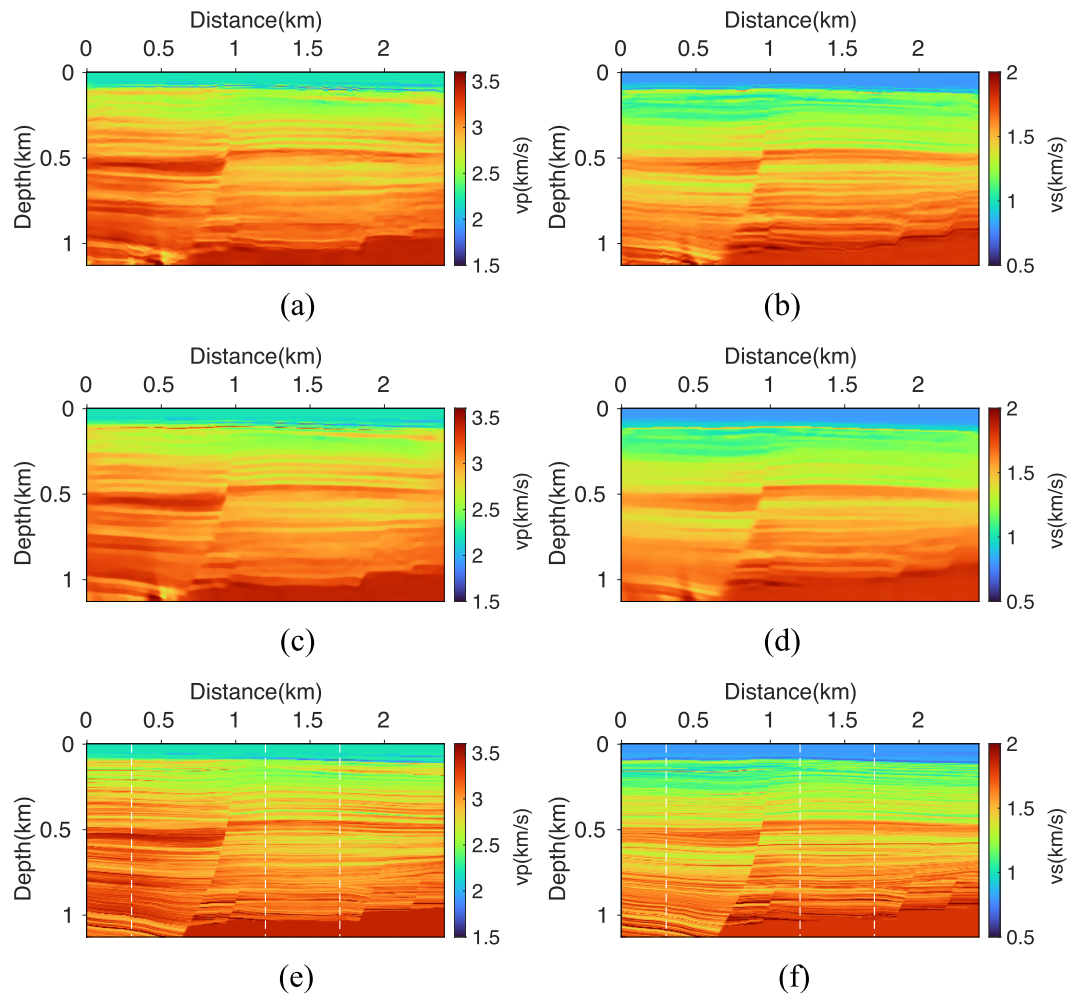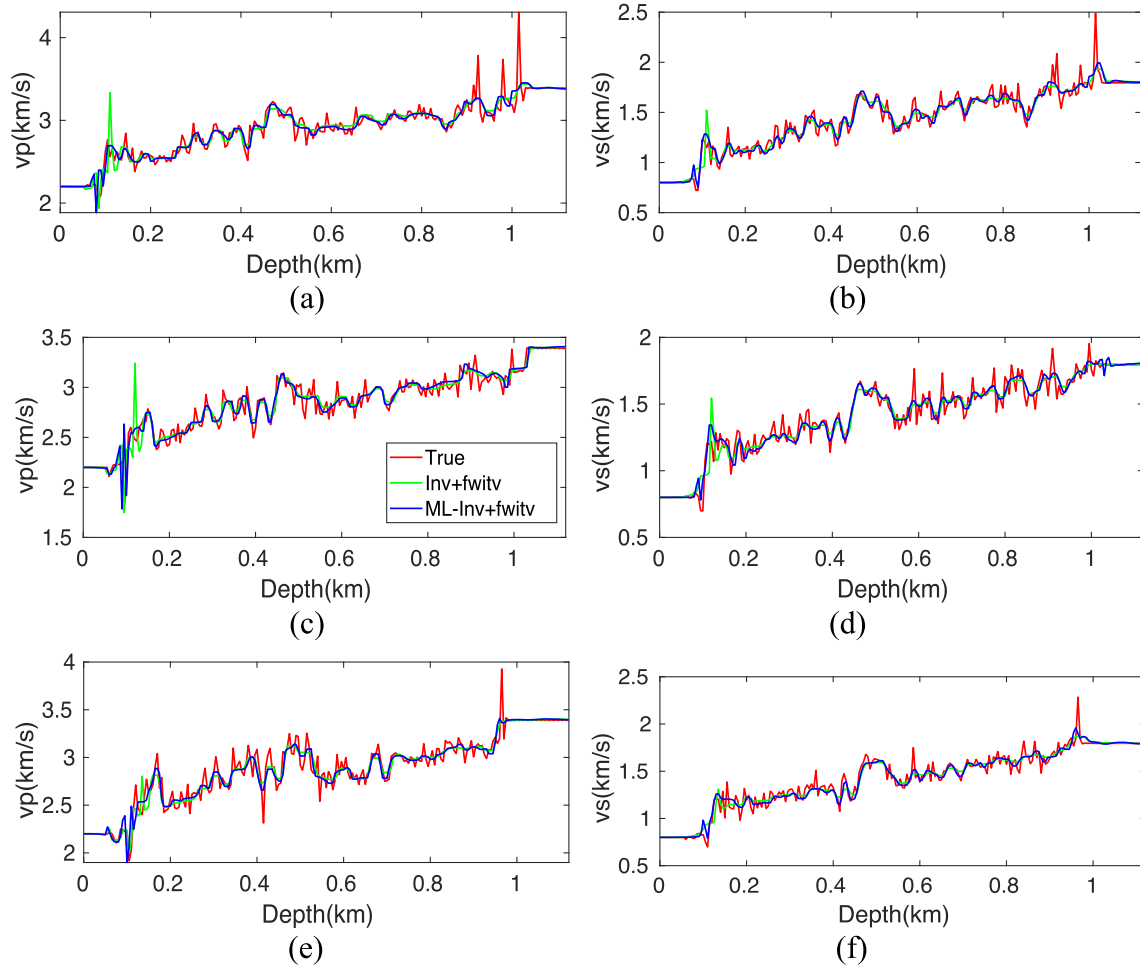
Figure 7. The EFWI results with TV regularization using a frequency band of 2–40 Hz starting from DNNs-aided EFWI result shown in Figs 3(g) and (h), (a) v_p and (b) v_s, and that starting from the conventional EFWI result shown in Figs 3(e) and (f), (c) v_p and (d) v_s. The true (e) v_p and (f) v_s model.

Otway synthetic example

We first apply the proposed method on a slice of the Otway model (Figs 3a and b). The synthetic model is generated for the CO2CRC Otway project, Australia. Distributions of its elastic properties were obtained from geostatistical interpolation between wells, and thus, the complexity of the synthetic model resembles a realistic subsurface model of the Otway site (Glubokovskikh *et al.* 2016). The size of the model used here is 2.4 km laterally, and 1.12 km in depth, with a grid interval of 5 m in both directions. 80 shots and 480 receivers are located evenly on the surface of the model to excite and record the two-component elastic wavefield, respectively. We use a Ricker wavelet with a 20 Hz peak frequency as the source wavelet. The recorded elastic data are generated by solving the 2-D elastic wave equation with a finite-difference scheme. We use the same modelling scheme and the same parameter settings in the simulations for elastic wave propagation in the EFWI. The initial model for the inversion is a smoothed version of the true model using a Gaussian smoothing window of 100 m width (Figs 3c and d). The initial model is not far from the true one, but does not include detailed structures. Thus, our objective is to test the performance of the proposed inversion algorithm in enhancing high-resolution components.

We first use the 2–15 Hz frequency band to implement conventional EFWI, and the inversion results after 80 iterations are shown in Figs 3(e) and (f). We can see that the spatial resolution is consistent with what we would expect from FWI for the band used, as the thin layers are hardly captured. The high-resolution model information is expected to be boosted by merging well logs with the seismic data in the proposed regularized EFWI. Three vertical profiles of the true model at 0.3, 1.2 and 1.7 km represent the well log information in this example. Their corresponding means and variances are computed in a 10-point (50 m) width Gaussian window. We interpret 20 facies from the three wells by manually grouping the means and variances. The means and variances of the inverted velocities (Figs 3e and f) at the well locations are computed with the same Gaussian window, and those provide the discriminate features for training the DNN. The pre-identified facies from the well logs are used as the labels in the training data set.

The neural network contains six hidden layers, having 256, 256, 128, 128, 64, 64 neurons, from left, input side, to right, output side. We apply SMOTE to augment the data set generated from the three vertical profiles at 0.3, 1.2 and 1.7 km to provide the required training and testing data sets, with a ratio of 8:2. We set the batch size and total training epochs to 128 and 6000, respectively, for

Figure 8. Comparison of v_p and v_s vertical profiles at distance of (a and b) 1 km, (c and d) 1.5 km and (e and f) 2 km. These profiles are not used as training wells. Red line: the true model, green line: the EFWI result with TV regularization shown in Figs 7(c) and (d) using 2–40 Hz starting from the conventional EFWI result, blue line: the EFWI result with TV regularization shown in Figs 7(a) and (b) using 2–40 Hz starting from the regularized EFWI result.
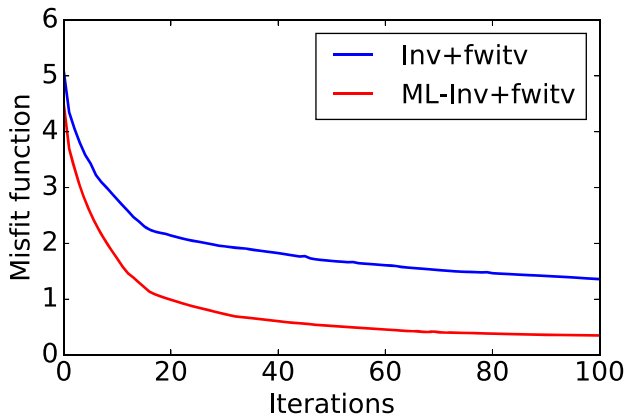

Figure 9. Evolution of the data misfit ($J_D(\mathbf{m})$) for the EFWI implementation using the 2–40 Hz frequency band starting from the conventional EFWI result in Figs 3(e) and (f) (blue line) and the regularized EFWI result in Figs 3(g) and (h) (red line). The number of iterations is 100.

optimizing the network parameters. Once the training process is finished, the network provides a statistical relationship between the inverted velocities (Figs 3e and f) and the interpreted facies labels. The history of the training and test accuracies are shown in Fig. 5;

these two accuracy curves converge to 92.16 and 74.57 per cent, respectively.

We then apply the trained network to the inverted model area to predict the mean and variance fields by a weighted average over facies. Actually, the conventional EFWI result delineates the means well because of a reasonably good starting model. Here, we show the predicted variance fields in Figs 6(a) and (b), which are crucial for recovering the high-resolution components. Figs 6(c) and (d) show the comparison of the variances at $x = 1.2$ km. We can see that the predicted variances using DNN are much closer to the true ones, while the variances computed from the conventional EFWI result are underestimated because of the limited frequency band. Figs 6(e) and (f) show the prior model recovered from the mean and variance fields, and they contain sufficient high-resolution model information thanks to the well-based-predicted variance field by using the neural network. Taking the balancing factor γ (eq. 7) as 0.5, the regularized EFWI result (Figs 3g and h) using the prior model contains enhanced details and higher-resolution components than the original FWI result. We then compare the regularized EFWI result (Figs 3g and h), the conventional EFWI result (Figs 3e and f) and the true model in more detail by showing their vertical profiles at distances of 1, 1.5 and 2 km in Fig. 4. Obviously, the regularized EFWI enriches the high-resolution information by incorporating the prior model into the inversion.
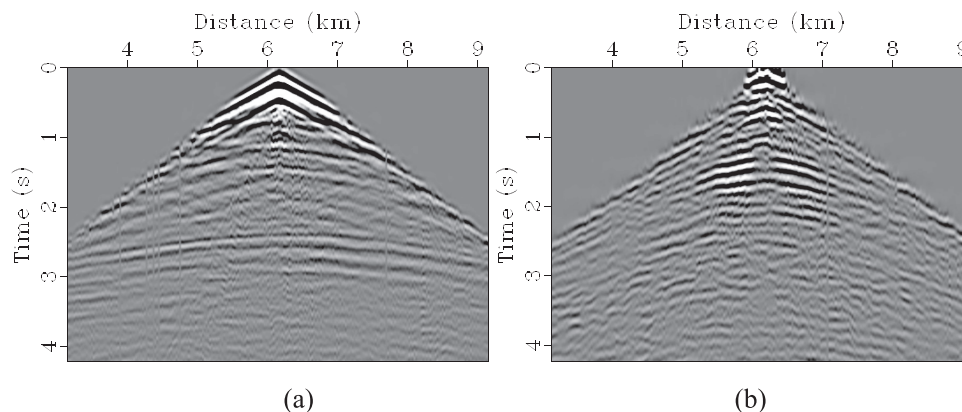
Figure 10. Volve OBC data set. (a) PP and (b) PS shot gathers for the source located at $x = 6.175$ km for the frequency band of 2–10 Hz.
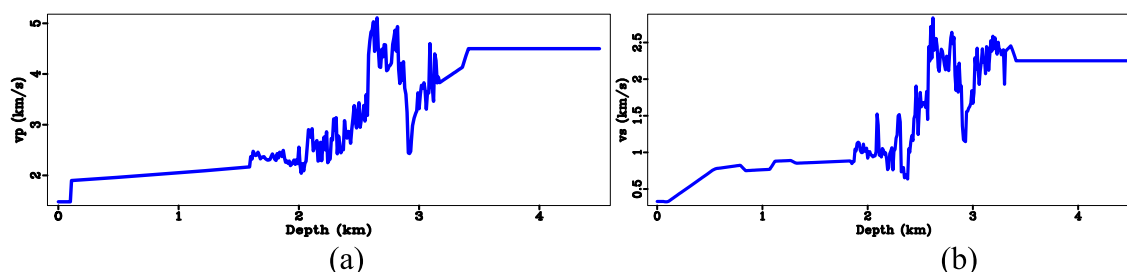
Figure 11. The well velocities after a slight calibration, (a) *P*-wave and (b) *S*-wave velocities. The well path is not vertical, starting from distance of about 8.0 km on the top to distance of 7.0 km on the bottom. The velocities between 1.6 and 3.4 km are obtained from sonic logs. The velocities at depth < 1.6 km and > 3.4 km are not available therefore they are generated by interpolation.

However, the seismic data matching does not necessarily improve because the regularization renders a steady introduction of the prior model information into the inversion to compete with the contribution of seismic data. Besides, the 2–15 Hz frequency band data are not that sensitive to the newly injected high-wavenumber components. In order to test whether the incorporated high-resolution components can be retained in the subsequent inversion and improve its data matching, we further implement EFWI with a TV regularization (Lin & Huang 2014) using higher frequencies of 2–40 Hz starting from the regularized EFWI result (Figs 3g and h) and the conventional EFWI result (Figs 3e and f), and their inversion results are shown in Figs 7(a) and (b), and (c) and (d), respectively. The inverted velocities shown in Figs 7(a) and (b) still delineate more details than that shown in Figs 7(c) and (d). For a detailed comparison, we also share the vertical profiles at locations 1, 1.5 and 2 km and include the true model for reference (Fig. 8). We can see that the inversion result using the prior model regularization is closer to the true model. The evolution of the data misfits during the EFWI implementations using the 2–40 Hz frequency band, shown in Fig. 9, indicates that the proposed method even improves the data matching.

Volve field example

We further verify the feasibility of the proposed method on a 2-D line of the OBC field data from Volve field in the Norwegian Central North Sea. The OBC seismic data include both primary (PP) and converted shear-wave (PS) data. Besides, there are available sonic log and check shot data for this oil field (Szydlik *et al.* 2007). Therefore, this field data set is a good candidate to test our method.

The model domain is 12.3 km laterally and 4.5 km in depth, and the grid interval is 10 m. A chalk layer is located in the inversion area which is characterized by a small dome-shaped structure (Szydlik *et al.* 2007). The 2-D line contains 240 receivers with 25 m interval, located at the water bottom. 121 shot gathers are used in the inversion, with a distance of 100 m between the shots, at a depth of 6 m. We were provided the pre-processed PP and PS data. The pre-processing of the PP and the PS data includes standard wavelet processing, noise and multiple attenuation techniques (Szydlik *et al.* 2007). Fig. 10 shows the shot gathers with a frequency band of 2–10 Hz for a source at location 6.175 km. Most of the direct and post-critical arrivals are muted, while the reflections are clear in the shot gathers with a maximum offset of about 5 km (Li *et al.* 2019). A slight calibration for the provided well log is required, because the well path is not vertical (Oh & Alkhalifah 2018). Fig. 11 shows the well velocities; the velocities between 1.6 and 3.4 km are obtained from sonic logs.

Figs 12(a) and (b) show the provided tomography-based velocity models. We smoothed the tomography model to serve as the starting model for EFWI (Figs 12c and d). The target reservoir at 3.0 km depth is obviously smeared. We use the frequency band 2–10 Hz in the inversion workflow. We first conduct the conventional EFWI by matching the seismic data, and the resulting model is shown in Figs 12(e) and (f). The reservoir with low velocities is delineated, but with limited resolution. We then interpret 10 facies from the provided well log and prepare the training data set to train the DNN. If we only use the estimated velocities at the well location to generate the training data set without data augmentation, the training process using such a data set hardly generalizes the accurate mathematical relationship between the input features and the interpreted facies.
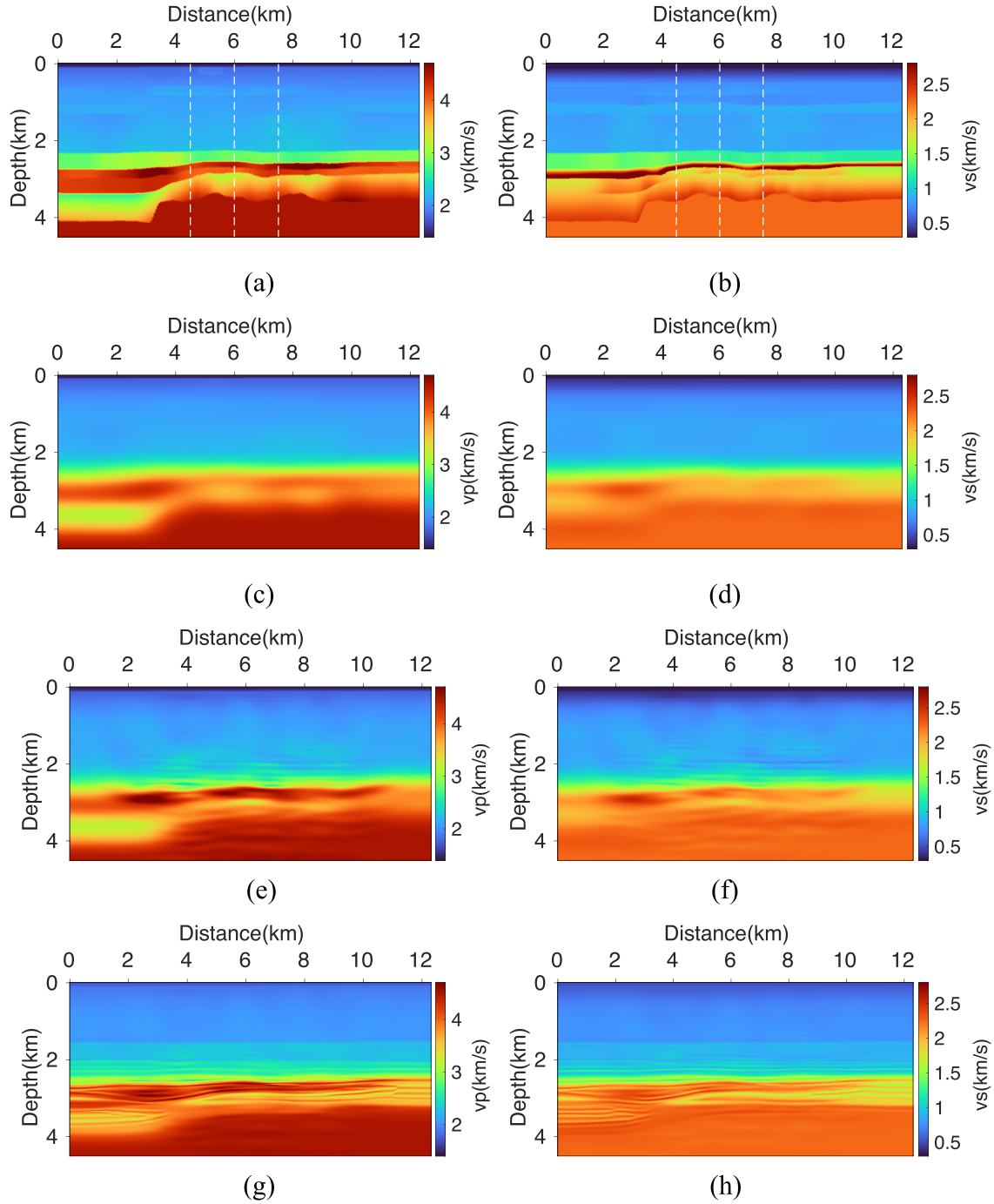
Figure 12. (a and b) The tomography v_p and v_s model for the Volve field data example, and the white dashed lines show the vertical profiles used for training. (c and d) The initial v_p and v_s model. (e and f) The conventional EFWI result: (e) v_p and (f) v_s. (g and h) The regularized EFWI result using the proposed method: (g) v_p and (h) v_s.

Therefore, three vertical profiles at 4.5, 6.0 and 7.5 km are used in the training process. The nearby well log and check-shot profiles are used to label facies for the training data set.

The designed DNN has 4 hidden layers with 64 neurons in each of them. We set the batch size and total training epochs as 128 and 6000 for optimizing the network parameters. The training and testing accuracies converge to 93.03 and 76.24 per cent, respectively. We then apply the prediction to the whole inverted model. The predicted means and variances of *P*-wave and *S*-wave velocities are shown in Figs 13(a) and (b), and (c) and (d), respectively. Then, the prior

model (Figs 13e and f) is recovered by matching the means and variances. Using the derived prior model, we conduct a regularized EFWI (Figs 12g and h) with the balancing factor $\gamma = 0.3$. The resolution is improved and the velocity model reveals more details of the reservoir. We also compare the vertical profiles of inverted velocities near the well with those from sonic logs as shown in Fig. 14. Although this vertical profile is not used for training, it is close to the vertical profile at $x = 7.5$ km that was used for training. Overall, the proposed method can improve the matching between the inverted and well velocities.
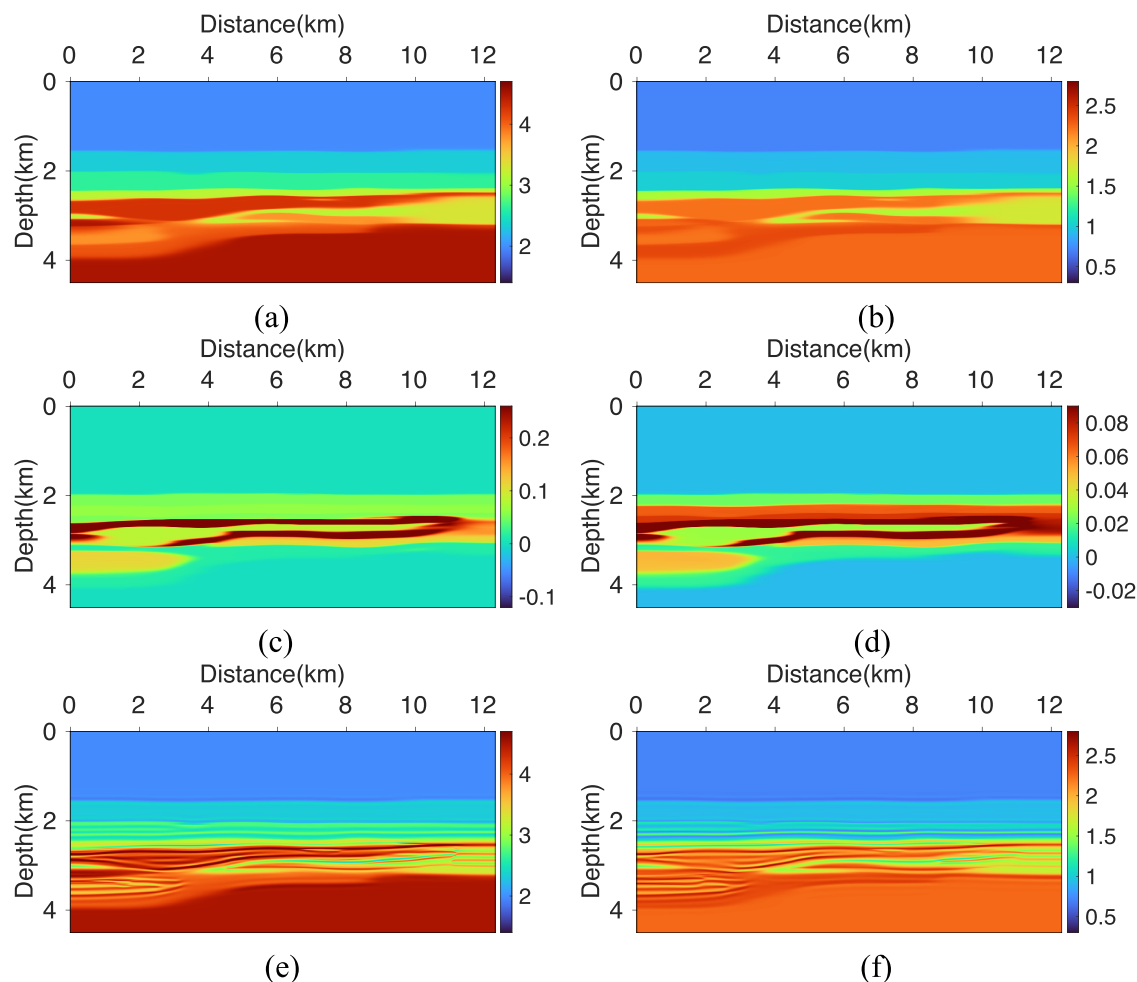
Figure 13. The predicted mean fields for (a) v_p and (b) v_s, the predicted variance fields for (c) v_p and (d) v_s, and the recovered prior model from the predicted mean and variance fields: (e) v_p and (f) v_s.
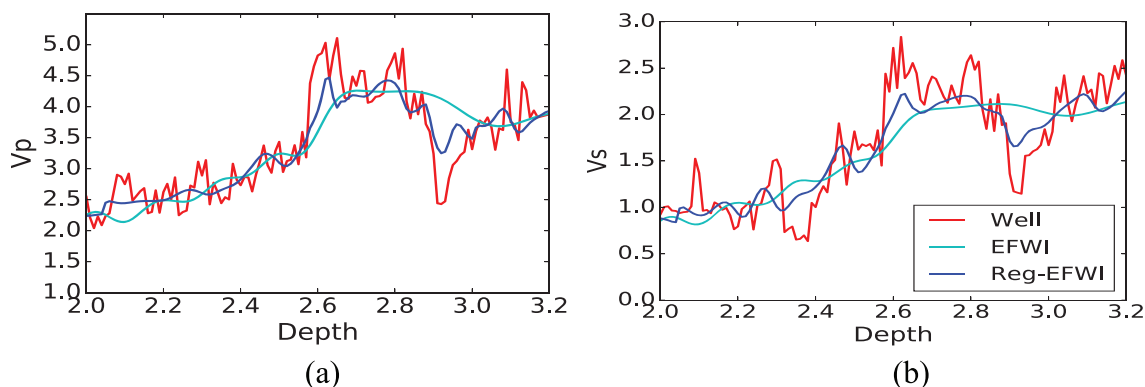
Figure 14. Comparison of (a) v_p and (b) v_s vertical profiles at the well location. Red line: the well velocity, green line: the conventional EFWI result in Figs 12(e) and (f), blue line: the regularized EFWI result in Figs 12(g) and (h) using the proposed method.

DISCUSSION

Seismic data and well logs provide crucial information from different perspectives in estimating the subsurface properties. Well logs directly measure the detailed properties of the subsurface, but with limited area range, while seismic data provide much larger coverage, but at a much lower resolution. To combine their merits, we incorporate well information into seismic waveform inversion using a DL-assisted regularization to enrich the model with more high-wavenumber components extracted from the well. Mathematically, the regularization parameter β, that balances the contributions from seismic data and prior knowledge, can be estimated automatically using the generalized cross-validation (GCV) and L-curve methods

(Hansen & OLeary 1993; Haber & Oldenburg 2000; Farquharson & Oldenburg 2004). Here, we select the parameter β by trial and error to incorporate the prior structures into the resulting model, while allowing a reasonably increase in the data misfits. The hyperparameter tuning is an important but challenging part for any DL application. We try potential sets of hyperparameters, which include the number of hidden layers and number of neurons in each layer, the learning rate, the activation function, and select the hyperparameter set that makes the training and testing accuracies, as much as possible, equally higher. For the DL part, the training step is the most time-consuming. The training in our examples required 20 minutes using a single GPU card. The additional computational cost arising from the regularization term is small.

The DNN method aims to learn the medium properties of the target zone from the training data set. The performance of the DNN is influenced by the quality of the training data set, which includes the inverted velocities near the wells and the labelled facies interpreted from the wells. A reasonable initially inverted model is necessary for predicting the prior information in the inversion zone, because they provide the DNN with input features. The most important required feature of the initially inverted model is its consistency over the model space. The edges of the model will often include illumination artefacts that are absent in the training of the DNN and that might induce errors in the prediction of the facies. More generally, if the well locations do not sample some subsurface features present in the model space, it might fail to deliver a satisfying prediction for the subsurface features uncovered by the wells. For complex subsurface media with strong heterogeneity, more wells are required to retrieve enough facies information. In addition, knowledge of the subsurface medium from other sources, such as geology, geostatistics, and so on, are expected to improve the facies interpretation. Moreover, these potential limitations mainly affect the preparation of the *a priori* model and in this case we may have to reduce the regularization weighting to allow for more data fitting.

We should also note that the synthetic example in this study are performed with noise-free seismic data and well logs. If the seismic data are contaminated with noise, the quality of the inversion result using solely the seismic data will be heavily affected by the noise. An appropriate regularization technique, such as Tikhonov and total variation (TV) regularization, should be applied to suppress the noise on the recovered model (Tikhonov *et al.* 2013). In addition, we should adjust the weighting parameter to rely more on the prior knowledge, which admits more constraints on the inversion in the proposed method with DL-assisted regularization. In this case, the noisy seismic data contributes less to the inversion, and therefore, the corresponding artefacts can be suppressed. We assume that the provided well information is reliable. It is worth mentioning that different amount of facies classes is interpreted from the well velocities in these two examples. As more facies are used, the statistical distribution of well velocities will be delineated more accurately. However, the complexity of the facies classification will increase, which imposes more challenges on the DNN-based facies classifier. We should balance these two extremes to determine the facies classes. The interpretation of facies is done here manually, and a more advanced automatic clustering approach deserves further studies.

We assume in this study that the subsurface medium is isotropic elastic with fixed density in this study. We only invert for the *P*- and *S*-wave velocities, and keep the density constant during the inversion. When density information is available, we should use it to avoid multiparameter trade-off, which often degrades inversion results of too many parameters (Köhn *et al.* 2012; Blom *et al.* 2017).

The regularization technique is expected to be helpful in mitigating this potential degradation because of the additional constraint from prior information. The field data set has anisotropy (Szydlik *et al.* 2007), and it can influence the performance of the inversion, which is based on an isotropy assumption. A good data matching at near and far offsets often cannot be achieved simultaneously without accounting for anisotropy. In the proposed methodology, the contribution from seismic data is competing with that from the prior model information from well logs to reduce the dependence of the inversion on seismic data. Therefore, the anisotropy effects on the inversion are somewhat suppressed. When the anisotropy properties are available from the well logs, the proposed method has the potential to extend to anisotropic EFWI. The prediction of the prior model for complex subsurface media should also combine more prior knowledge from other sources and disciplines to enhance the prediction accuracy.

When well logs are available along with seismic data in the inversion region, the proposed method can boost the resolution and illumination by combining the well information with the seismic data using a deep-learning assisted regularization. The proposed method can be extended to more complex media, for example, 3-D anisotropic media, but might require more well information. This can be a future topic of research.

CONCLUSIONS

We developed a deep learning assisted regularization algorithm to push the resolution limit of regular EFWI. A DNN is used to learn the statistical relation between the inverted model from an initial EFWI implementation and facies extracted from well logs. The mean and variance of the velocities, calculated within a Gaussian window along the well, are utilized as the discriminant features for the facies. Thus, the high-resolution well information is preserved by including the variance into the facies features. The resulting high-resolution prior model, recovered from the predicted mean and variance fields, enhances the subsequent inversion resolution and illumination as we use it as a model regularizer term in EFWI. The numerical examples show that the proposed method improves the model resolution and consistency with well logs.

ACKNOWLEDGEMENTS

DATA AVAILABILITY

The data underlying this paper will be shared on reasonable request to the corresponding author.

REFERENCES

Alkhalifah, T., 2014. Scattering-angle based filtering of the waveform inversion gradients, *Geophys. J. Int.,* **200**(1), 363–373.

Alkhalifah, T., 2016. Full-model wavenumber inversion: an emphasis on the appropriate wavenumber continuation, *Geophysics,* **81**(3), R89–R98.

Aragao, O. & Sava, P., 2020. Elastic full waveform inversion with probabilistic petrophysical clustering, *Geophys. Prospect.,* **68**(4), 1341–1355.

Araya-Polo, M., Farris, S. & Florez, M., 2019. Deep learning-driven velocity model building workflow, *Leading Edge,* **38**(11), 872a1–872a9.

Asnaashari, A., Brossier, R., Garambois, S., Audebert, F., Thore, P. & Virieux, J., 2013. Regularized seismic full waveform inversion with prior model information, *Geophysics,* **78**(2), R25–R36.

Bamberger, A., Chavent, G., Hemon, C. & Lailly, P., 1982. Inversion of normal incidence seismograms, *Geophysics,* **47,** 757–770.

Bergen, K.J., Johnson, P.A., Maarten, V. & Beroza, G.C., 2019. Machine learning for data-driven discovery in solid Earth geoscience, *Science,* 363(6433), doi:10.1126/science.aau0323.

Blom, N., Boehm, C. & Fichtner, A., 2017. Synthetic inversions for density using seismic and gravity data, *Geophys. J. Int.,* **209**(2), 1204–1220.

Bosch, M., Carvajal, C., Rodrigues, J., Torres, A., Aldana, M. & Sierra, J., 2009. Petrophysical seismic inversion conditioned to well-log data: methods and application to a gas reservoir, *Geophysics,* **74**(2), O1–O15.

Bosch, M., Mukerji, T. & Gonzalez, E.F., 2010. Seismic inversion for reservoir properties combining statistical rock physics and geostatistics: a review, *Geophysics,* **75**(5), 75A165–75A176.

Buland, A. & Omre, H., 2003, Bayesian linearized AVO inversion, *Geophysics,* **68**(1), 185–198.

Bunks, C., Saleck, F.M., Zaleski, S. & Chavent, G., 1995. Multiscale seismic waveform inversion, *Geophysics,* **60**(5), 1457–1473.

Byrd, R.H., Lu, P., Nocedal, J. & Zhu, C., 1995. A limited memory algorithm for bound constrained optimization, *SIAM Journal on scientific computing,* **16**(5), 1190–1208.

Chawla, N.V., Bowyer, K.W., Hall, L.O. & Kegelmeyer, W.P., 2002. SMOTE: synthetic minority over-sampling technique, *J. Artif. Intell. Res.,* **16,** 321–357.

Curtis, A. & Lomax, A., 2001. Prior information, sampling distributions, and the curse of dimensionality, *Geophysics,* **66**(2), 372–378.

Dai, H. & MacBeth, C., 1995. Automatic picking of seismic arrivals in local earthquake data using an artificial neural network, *Geophys. J. Int.,* **120**(3), 758–774.

Das, V., Pollack, A., Wollner, U. & Mukerji, T., 2019. Convolutional neural network for seismic impedance inversion, *Geophysics,* **84**(6), R869–R880.

Dowla, F.U., Taylor, S.R. & Anderson, R.W., 1990. Seismic discrimination with artificial neural networks: preliminary results with regional spectral data, *Bull. seism. Soc. Am.,* **80**(5), 1346–1373.

Dysart, P.S. & Pulli, J.J., 1990. Regional seismic event classification at the NORESS array: seismological measurements and the use of trained neural networks, *Bull. seism. Soc. Am.,* **80**(6B), 1910–1933.

Eidsvik, J., Avseth, P., Omre, H., Mukerji, T. & Mavko, G., 2004. Stochastic reservoir characterization using prestack seismic data, *Geophysics,* **69**(4), 978–993.

Fanchi, J.R., 2002. *Shared Earth Modeling: Methodologies for Integrated Reservoir Simulations,* Gulf Professional Publishing, pp. 170–181.

Farquharson, C.G. & Oldenburg, D.W., 2004. A comparison of automatic techniques for estimating the regularization parameter in non-linear inverse problems. *Geophys. J. Int.,* **156**(3), 411–425.

Gao, D., 2011. Latest developments in seismic texture analysis for subsurface structure, facies, and reservoir characterization: a review, *Geophysics,* **76**(2), W1–W13.

Gauthier, O., Virieux, J. & Tarantola, A., 1986. Two-dimensional nonlinear inversion of seismic waveforms: numerical results, *Geophysics,* **51**(7), 1387–1403.

Glubokovskikh, S., Pevzner, R., Dance, T., Caspari, E., Popik, D., Shulakova, V. & Gurevich, B., 2016. Seismic monitoring of CO_2 geosequestration: CO2CRC Otway case study using full 4D FDTD approach, *Int. J. Greenh. Gas Control.,* **49,** 201–216.

Grana, D., 2016. Bayesian linearized rock-physics inversion, *Geophysics,* **81**(6), D625–D641.

Haber, E. & Oldenburg, D.W., 2000. A GCV based method for nonlinear ill-posed problems, *Comput. Geosci.,* **4,** 41–63.

Hansen, P. C. & OLeary, D. P., 1993. The use of the L-curve in the regularization of discrete ill-posed problems, *SIAM J. Sci. Comput.,* **14,** 1487–1503.

Kazei, V., Ovcharenko, O., Plotnitskii, P., Peter, D., Zhang, X. & Alkhalifah, T.A., 2019. Mapping seismic data cubes to vertical velocity profiles

by deep learning: new full-waveform inversion paradigm? *Geophysics,* submitted.

Kingma, D.P. & Ba, J., 2014. Adam: a method for stochastic optimization. arXiv:1412.6980.

Köhn, D., De Nil, D., Kurzmann, A., Przebindowska, A. & Bohlen, T., 2012. On the influence of model parametrization in elastic full waveform tomography, *Geophys. J. Int.,* **191**(1), 325–345.

Kortström, J., Uski, M. & Tiira, T., 2016. Automatic classification of seismic events within a regional seismograph network, *Comput. Geosci.,* **87,** 22–30.

Lailly, P., 1983. The seismic inverse problem as a sequence of before stack migrations, in *Conference on Inverse Scattering, Theory and Application,* SIAM, Expanded Abstracts, pp. 206–220.

LeCun, Y., Bengio, Y. & Hinton, G., 2015. Deep learning, *Nature,* **521**(7553), 436–444.

Lin, Y. & Huang, L., 2014. Acoustic-and elastic-waveform inversion using a modified total-variation regularization scheme, *Geophys. J. Int.,* **200**(1), 489–502.

Li, Y., Alkhalifah, T. & Guo, Q., 2021. Target-oriented time-lapse waveform inversion using deep learning assisted regularization, *Geophysics,* doi:10.1190/geo2020-0383.1.

Li, Y., Alkhalifah, T. & Zhang, Z., 2020. High-resolution regularized elastic full waveform inversion assisted by deep learning, in *82nd EAGE Annual International Meeting, Expanded Abstracts,* pp. 1–5.

Li, Y., Biondi, B., Clapp, R. & Nichols, D., 2016. Integrated VTI model building with seismic data, geologic information, and rock-physics modeling—Part 1: theory and synthetic test, *Geophysics,* **81**(5), C177–C191.

Li, Y., Choi, Y., Alkhalifah, T., Li, Z. & Zhang, K., 2018. Full-waveform inversion using a nonlinearly smoothed wavefield, *Geophysics,* **83**(2), R117–R127.

Li, Y., Guo, Q., Li, Z. & Alkhalifah, T., 2019. Elastic reflection waveform inversion with variable density, *Geophysics,* **84**(4), R553–R567.

Naeini, E.Z., Alkhalifah, T., Tsvankin, I., Kamath, N. & Cheng, J., 2016. Main components of full-waveform inversion for reservoir characterization, *First Break,* **34**(11), 37–48.

Nair, V. & Hinton, G. E., 2010. Rectified linear units improve restricted boltzmann machines, in *P roceedings of the 27th International Conference on Machine Learning (ICML-10),* Haifa, Israel, pp. 807–814.

Oh, J.W. & Alkhalifah, T., 2018. Full waveform inversion using envelope-based global correlation norm, *Geophys. J. Int.,* **213**(2), 815–823.

Ovcharenko, O., Kazei, V., Kalita, M., Peter, D. & Alkhalifah, T., 2019. Deep learning for low-frequency extrapolation from multioffset seismic data, *Geophysics,* **84**(6), R989–R1001.

Pratt, R.G., Shin, C. & Hick, G.J., 1998. Gauss–Newton and full Newton methods in frequency–space seismic waveform inversion, *Geophys. J. Int.,* **133**(2), 341–362.

Qian, F., Yin, M., Liu, X.Y., Wang, Y.J., Lu, C. & Hu, G.M., 2018. Unsupervised seismic facies analysis via deep convolutional autoencoders, *Geophysics,* **83**(3), A39–A43.

Richardson, A., 2018. Seismic full-waveform inversion using deep learning tools and techniques, arXiv:1801.07232.

Routh, P. *et al.,* 2017. Impact of high-resolution FWI in the Western Black Sea: revealing overburden and reservoir complexity, *Leading Edge,* **36**(1), 60–66.

Schmidhuber, J., 2015. Deep learning in neural networks: an overview, *Neural networks,* **61,** 85–117.

Singh, S., Tsvankin, I. & Naeini, E.Z., 2018. Bayesian framework for elastic full-waveform inversion with facies information, *Leading Edge,* **37**(12), 924–931.

Sirgue, L. & Pratt, R.G., 2004. Efficient waveform inversion and imaging: a strategy for selecting temporal frequencies, *Geophysics,* **69**(1), 231–248.

Song, C., Alkhalifah, T. & Li, Y., 2020. A sequential inversion with outer iterations for the velocity and the intrinsic attenuation using an efficient wavefield inversion, *Geophysics,* **85**(6), R447–R459.

Srivastava, N., Hinton, G., Krizhevsky, A., Sutskever, I. & Salakhutdinov, R., 2014. Dropout: a simple way to prevent neural networks from overfitting, *J. Mach. Learn. Res.,* **15,** 1929–1958.

Szydlik, T., Smith, P., Way, S., Aamodt, L. & Friedrich, C., 2007. 3D PP/PS prestack depth migration on the Volve field, *First Break,* **25**:43–47.

Tarantola, A., 1984. Inversion of seismic reflection data in the acoustic approximation, *Geophysics,* **49**, 1259–1266.

Tikhonov, A.N., Goncharsky, A.V., Stepanov, V.V. & Yagola, A.G., 2013. *Numerical methods for the solution of ill-posed problems,* Vol. 328, Springer Science & Business Media.

Van Leeuwen, T. & Herrmann, F.J., 2013. Mitigating local minima in full-waveform inversion by expanding the search space, *Geophys. J. Int.,* **195**(1), 661–667.

Veeken, P.C. & Rauch-Davies, M., 2006. AVO attribute analysis and seismic reservoir characterization, *First Break,* **24**(2), 41–52.

Vigh, D., Jiao, K., Watts, D. & Sun, D., 2014. Elastic full-waveform inversion application using multicomponent measurements of seismic data collection, *Geophysics,* **79**(2), R63–R77.

Virieux, J., 1986. P-SV wave propagation in heterogeneous media: velocity-stress finite-difference method, *Geophysics,* **51**(4), 889–901.

Virieux, J. & Operto, S., 2009. An overview of full-waveform inversion in exploration geophysics, *Geophysics,* **74**(6), WCC1–WCC26.

Wang, C., Yingst, D., Bai, J., Leveille, J., Farmer, P. & Brittan, J., 2013. Waveform inversion including well constraints, anisotropy, and attenuation, *Leading Edge,* **32**(9), 1056–1062.

Warner, M. & Guasch, L., 2016. Adaptive waveform inversion: theory, *Geophysics,* **81**(6), R429–R445.

Wu, B., Meng, D., Wang, L. & Liu, N., 2020. Seismic impedance inversion using fully convolutional residual network and transfer learning, *IEEE Geosci. Remote Sens. Lett.,* **17**, 12, 2140–2144

Wu, R.S., Luo, J. & Wu, B., 2014. Seismic envelope inversion and modulation signal model, *Geophysics,* **79**(3), WA13–WA24.

Yang, F. & Ma, J., 2019. Deep-learning inversion: a next generation seismic velocity model building method, *Geophysics,* **84**(4), 1–133.

Zabihi Naeini, E. & Exley, R., 2017. Quantitative interpretation using facies-based seismic inversion, *Interpretation,* **5**(3), SL1–SL8.

Zhang, W. & Shen, Y., 2010. Unsplit complex frequency-shifted PML implementation17 using auxiliary differential equations for seismic wave modeling, *Geophysics,* **75**(4), T141–T154.

Zhang, Z. & Alkhalifah, T., 2019b. Regularized elastic full waveform inversion using deep learning, *Geophysics,* **84**(5), 1–47.

Zhang, Z. & Alkhalifah, T., 2020. High-resolution reservoir characterization using deep learning aided elastic full-waveform inversion: the North Sea field data example, *Geophysics,* **85**(4), WA137–WA146.

Zhang, Z.D. & Alkhalifah, T., 2019a. Local-crosscorrelation elastic full-waveform inversion, *Geophysics,* **84**(6), R897–R908.

Zhang, Z.D., Alkhalifah, T., Naeini, E.Z. & Sun, B., 2018. Multiparameter elastic full waveform inversion with facies-based constraints, *Geophys. J. Int.,* **213**(3), 2112–2127.

Zhao, T., Li, F. & Marfurt, K.J., 2017. Constraining self-organizing map facies analysis with stratigraphy: an approach to increase the credibility in automatic seismic facies classification, *Interpretation,* **5**(2), T163–T171.

Zunino, A., Mosegaard, K., Lange, K., Melnikova, Y. & Mejer Hansen, T., 2015. Monte Carlo reservoir analysis combining seismic reflection data and informed priors, *Geophysics,* **80**(1), R31–R41.